Chinese Chemical Letters 36 (2025) 110491

Contents lists available at ScienceDirect

Chinese Chemical Letters

journal homepage: www.elsevier.com/locate/cclet

Oxygen vacancies-rich molybdenum tungsten oxide nanowires as a highly active nitrogen fixation electrocatalyst

Jincheng Zhang[1], Mengjie Sun[1], Jiali Ren[1], Rui Zhang, Min Ma, Qingzhong Xue*, Jian Tian*

School of Materials Science and Engineering, Shandong University of Science and Technology, Qingdao 266590, China

ARTICLE INFO

Article history:
Received 21 June 2024
Revised 21 September 2024
Accepted 22 September 2024
Available online 26 September 2024

Keywords:
Electrocatalytic N_2 reduction reaction
Molybdenum-tungsten oxide
Nanowires
Oxygen vacancies
Non-noble metal

ABSTRACT

Herein, vacancy engineering is utilized reasonably to explore molybdenum tungsten oxide nanowires (W_4MoO_3 NWs) rich in O-vacancies as an advanced electrochemical nitrogen reduction reaction (eNRR) electrocatalyst, realizing further enhancement of NRR performance. In 0.1 mol/L Na_2SO_4, W_4MoO_3 NWs rich in O vacancies (CTAB-D-W_4MoO_3) achieve a large NH_3 yield of 60.77 μg h^{-1} $mg^{-1}_{cat.}$ at -0.70 V *vs.* RHE and a high faradaic efficiency of 56.42% at -0.60 V, much superior to the W_4MoO_3 NWs deficient in oxygen vacancies (20.26 μg h^{-1} $mg^{-1}_{cat.}$ and 17.1% at -0.70 V *vs.* RHE). Meanwhile, W_4MoO_3 NWs rich in O-vacancies also show high electrochemical stability. Density functional theory (DFT) calculations present that O vacancies in CTAB-D-W_4MoO_3 reduce the energy barrier formed by the intermediate of *N-NH, facilitate the activation and further hydrogenation of *N-N, promote the NRR process, and improve NRR activity.

Ammonia (NH_3), as an industrial raw material can produce explosives, plastics, synthetic fibers, resins, and many other industrial compounds [1-3]. NH_3 can also be used as a promising carrier for carbon-free energy storage and conversion [4]. However, the inherent properties of strong N≡N bonds make N_2 extremely difficult to synthesize NH_3 from the hydrogenation of N_2 in the atmosphere [5-8], So far, industrial NH_3 production still relies mainly on the traditional Haber-Bosch method. However, this process needs a large amount of energy and produces a large amount of carbon dioxide [9-11]. Therefore, developing green and sustainable routes to achieve efficient fixation of N_2 under milder conditions is urgent.

Electrochemical nitrogen reduction reaction (eNRR) is carried out using renewable electricity, which is considered a promising option for artificially fixing N_2 [12,13]. However, NRR must be driven by an effective electrocatalyst. Although the noble metal-based catalysts (Ru, Pd, Ag Au [14-17], *etc.*) exhibit good NRR activity, their low abundance and high cost hinder large-scale application [18,19]. Therefore, researchers have given considerable attention to Earth-abundant alternatives.

Transition metal oxides (TMOs) are considered important NRR catalysts due to their structural adjustability, rich redox properties, and earth abundance [20,21]. Therefore, developing high-performance TMOs catalysts through specific adjustments has great potential. Among these TMOs, tungsten trioxide (WO_3) has attracted extensive research interest due to its wide range of applications, high electrochemical stability, and abundant supply [22]. In addition, Density functional theory (DFT) calculation has also shown that W has the potential to activate the nitrogen-nitrogen triple bond, which can lead to the nitrogen reduction reaction [23]. However, due to the lack of active sites and limited electrical conductivity of WO_3, its NRR catalytic effect is poor [24]. As an important element in biological nitrogenase, Mo is used to catalytically fix N_2 in biological systems [25]. Studies on some Mo-based catalysts (MoS_2 [26], MoO_3 [25], Mo_2N [27], and even Mo monoatomic catalysts [28]) have shown that Mo is the active center of immobilized N_2. It helps stabilize -N_2H_y intermediates (-N_2H, -N_2H_2, *etc.*). and desorb -NH_2 species during NRR [29,30]. Therefore, by adding MoO_3, introducing Mo elements and adjusting the local atomic structure to generate more active sites, the electrochemical NRR activity is enhanced. In addition, oxygen vacancies (OVs), constructed on TMOs, can act as electron trapping centers for π-backdonation of N_2 molecules, improving the electrochemical activity and electrical conductivity, promoting energetics and kinetics of NRR reaction [31].

Herein, we report the synthesis of artificial NH_3 under environmental conditions using 1D OVs-rich molybdenum-tungsten bimetallic oxide nanowires (CTAB-D-W_4MoO_3 NWs) as active and selective electrocatalysts. CTAB-D-W_4MoO_3 NWs realize a large NH_3 yield of 60.77 μg h^{-1} $mg^{-1}_{cat.}$ at −0.70 V *vs.* RHE and a high

* Corresponding authors.
E-mail addresses: xueqz@upc.edu.cn (Q. Xue), jiantian@sdust.edu.cn (J. Tian).
[1] These authors contributed equally to this work.

https://doi.org/10.1016/j.cclet.2024.110491
1001-8417/

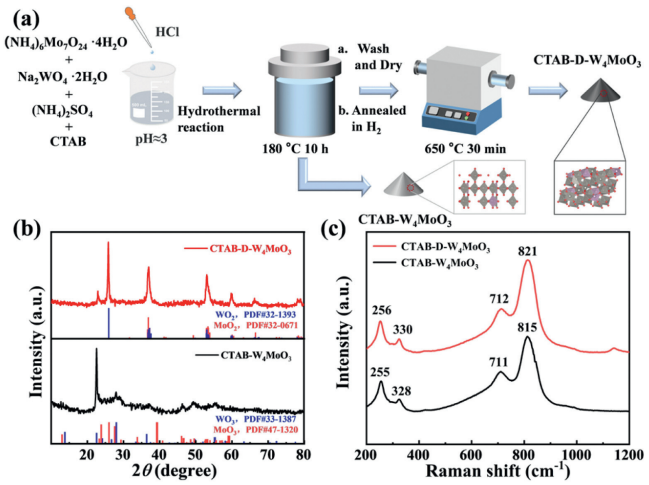

Fig. 1. (a) The schematic synthesis diagram of W_4MoO_3 nanowires deficient in oxygen vacancies (CTAB-W_4MoO_3) and W_4MoO_3 nanowires rich in O-vacancies (CTAB-D-W_4MoO_3 NWs). (b) XRD patterns and (c) Raman spectra of CTAB-W_4MoO_3 and CTAB-D-W_4MoO_3.

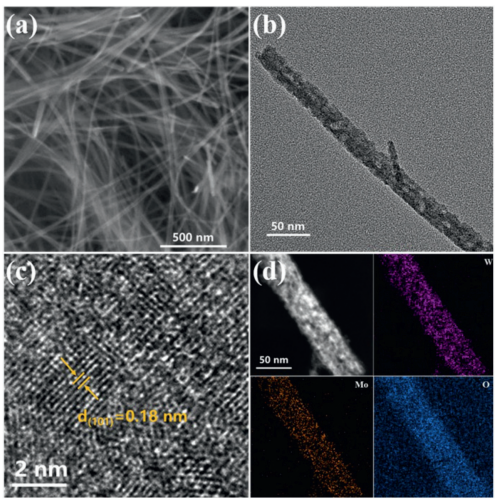

Fig. 2. (a) Scanning electron microscope (SEM), (b) TEM, (c) high resolution transmission electron microscope (HRTEM), and (d) corresponding EDS elemental mapping images of CTAB-D-W_4MoO_3.

faradaic efficiency (FE) of 56.42% at −0.60 V, much superior to molybdenum-tungsten bimetallic oxide nanowires deficient in OVs (CTAB-W_4MoO_3 NWs: 20.26 μg h^{-1} $mg^{-1}{}_{cat.}$ and 17.1%). In addition, CTAB-D-W_4MoO_3 NWs exhibit excellent cyclic stability and long-term stability.

W_4MoO_3 nanowires rich in O-vacancies (CTAB-D-W_4MoO_3 NWs) were obtained using ammonium molybdate tetrahydrate as Mo source and sodium tungstate dihydrate as W source. Fig. 1a shows the synthesis strategy of CTAB-D-W_4MoO_3 NWs. Firstly, pure W_4MoO_3 NWs were prepared, and the surfactant cetyltrimethylammonium bromide was added to avoid product aggregation. Then, W_4MoO_3 NWs with abundant O vacancies were acquired via annealing under an H_2 atmosphere. The local atomic structure is changed and abundant oxygen defects are formed in W_4MoO_3 owing to the reducibility of H_2. These defect sites provide more active sites for N_2 adsorption, and enhance the electron transport rate of the reaction. The improvement of catalyst nitrogen fixation performance is precisely owing to the large specific surface area and the catalyst defects. In this article, the catalyst samples before and after annealing are named CTAB-W_4MoO_3 and CTAB-D-W_4MoO_3 [24].

The crystal structures of CTAB-D-W_4MoO_3 and CTAB-W_4MoO_3 were tested by X-ray diffraction (XRD) (Fig. 1b). The precursor (CTAB-W_4MoO_3) is mainly composed of MoO_3 (PDF #47–1320) and WO_3 (PDF #33–1387). After annealing, CTAB-D-W_4MoO_3 is mainly composed of MoO_2 (PDF #32–0671) and WO_2 (PDF #32–1393). Although masked by stronger dioxide peaks, peaks of MoO_3 and WO_3 are still present, suggesting the formation of oxygen vacancies following calcination. In contrast, the XRD pattern of CTAB-H-W_4MoO_3 is similar to that of CTAB-W_4MoO_3 except for the difference in peak intensity, which further confirms the existence of oxygen vacancies in the catalyst (Fig. S1 in Supporting information). For Raman spectra (Fig. 1c), it can be seen that the characteristic peaks of CTAB-W_4MoO_3 and CTAB-D-W_4MoO_3 are similar. The bands at 712 and 821 cm^{-1} correspond to the stretching mode of M-O-M (M represents metal). The bands at 326 and 263 cm^{-1} are ascribed to the O-M-O bending mode, suggesting the presence of metal oxides in the catalysts [32]. Yet, the relatively wide peak of CTAB-D-W_4MoO_3 indicates the possibility of O vacancies in W_4MoO_3 [24].

The survey X-ray photoelectron spectroscopy (XPS) spectrum of CTAB-D-W_4MoO_3 (Fig. S2 in Supporting information) shows the presence of W, Mo, and O elements in the sample. Fig. S3a (Supporting information) shows the W 4f spectrum of CTAB-D-W_4MoO_3 and CTAB-W_4MoO_3 nanowires. CTAB-D-W_4MoO_3 not only has peaks of W^{6+} (35.80 and 38.12 eV, 40.57 eV-satellite peak), but also peaks of W^{5+} (35.17 and 37.31 eV) and W^{4+} (32.76 and 34.88 eV) [33]. This is because W^{6+} undergoes the reduction of oxide during heat treatment in H_2 atmosphere, forming O vacancies in the catalysts [34]. Similarly, in the Mo 3d spectrum (Fig. S3b in Supporting information), the peaks at 231.93 and 235.37 eV are ascribed to Mo^{6+} $3d_{5/2}$ and $3d_{3/2}$, respectively, while the peaks at 229.15 and 232.59 eV correspond to Mo^{4+} $3d_{5/2}$ and $3d_{3/2}$, respectively [35]. The O 1s spectrum in Fig. S3c (Supporting information) further indicates the formation of oxygen vacancies. The main peak at 530.28 eV is attributed to the oxygen metallic bond of O-W or O-Mo [36]. Importantly, another peak is clearly observed at 531.82 eV, corresponding to oxygen vacancies [36]. Furthermore, the peak at 533.26 eV is ascribed to the C–O bond [24]. As shown in Fig. S3d (Supporting information), the electron paramagnetic resonance (EPR) signal intensity of CTAB-D-W_4MoO_3 NWs is significantly higher than CTAB-W_4MoO_3 NWs, suggesting the presence of vacancies in CTAB-D-W_4MoO_3 NWs. For CTAB-D-W_4MoO_3 NWs, the noticeable signal with a g value of 2.002 is caused by oxygen vacancies. Combined with XPS analysis, the existence of oxygen vacancies in the prepared CTAB-D-W_4MoO_3 NWs can be confirmed.

As shown in Fig. S4 (Supporting information), the precursor of the hydrothermal product CTAB-W_4MoO_3 presents the nanowire morphology. After annealing, CTAB-D-W_4MoO_3 preserves the nanowire structure (Fig. 2a). The transmission electron microscope (TEM) image further confirms this observation (Fig. S5 in Supporting information), and the diameter of the nanowire is about 20 nm (Fig. 2b). In addition, the 0.18 nm lattice fringe corresponds to the (101) crystal plane of WO_{3-x} or MoO_{3-x} (Fig. 2c). Moreover, the energy dispersive spectroscopy (EDS) elemental mapping images show that Mo, W, and O are uniformly distributed across the nanowires (Fig. 2d). The contents of Mo and W in catalyst were measured by inductively coupled plasma mass spectrometry (ICP-MS) (Table S1 in Supporting information).

The NRR activity of CTAB-D-W_4MoO_3 was further evaluated in an H-type electrolytic cell containing 0.1 mol/L Na_2SO_4. Considering that there may be a few NO_x impurities in the electrolyte, we first detect NO_3^- and NO_2^- in the electrolyte before and after introducing N_2 for 30 min. The corresponding UV visible spectrum is shown in Fig. S6 (Supporting information). The presence of NO_3^- and NO_2^- is not found, suggesting that the experimental results

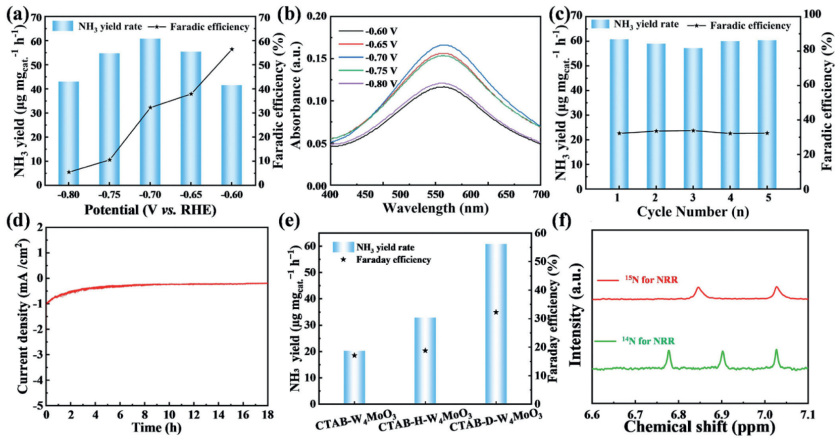

Fig. 3. (a) NH_3 yields and FEs of CTAB-D-W_4MoO_3 at a series of potentials. (b) UV–vis absorption spectra of 0.1 mol/L Na_2SO_4 after 2 h electrolysis on CTAB-D-W_4MoO_3. (c) NH_3 yields and FEs of CTAB-D-W_4MoO_3 at −0.70 V during recycling tests. (d) Time-dependent current density curves of CTAB-D-W_4MoO_3 for NRR at −0.70 V. (e) NH_3 yields and FEs of CTAB-D-W_4MoO_3 CTAB-H-W_4MoO_3 and CTAB-W_4MoO_3. (f) ^1H NMR spectra of the electrolyte after NRR using $^{15}N_2$ and $^{14}N_2$ as the nitrogen source, respectively.

are not affected by impurity contamination. Watt/Chrisp and indophenols blue method were used to gage the amount of possible by-product N_2H_4 and produced NH_3, and corresponding calibration curves were shown in Fig. S7 (Supporting information). Firstly, CTAB-D-W_4MoO_3 samples were tested in N_2 and Ar saturated 0.1 mol/L Na_2SO_4. From Fig. S8 (Supporting information), it can be seen that the current density of CTAB-D-W_4MoO_3 sample in N_2-saturated 0.1 mol/L Na_2SO_4 shows a significant difference from that in Ar-saturated electrolyte, mainly due to the presence of nitrogen reduction reaction. Subsequently, a further systematic study was conducted on the electrocatalytic NRR performance of CTAB-D-W_4MoO_3 samples in 0.1 mol/L Na_2SO_4 within −0.6 V to −0.8 V *vs.* RHE. Fig. 3a shows the average ammonia production rate and Faraday efficiency of CTAB-D-W_4MoO_3 samples running chronoamperometry testing for 2 h, calculated according to formulas. Fig. 3b shows the UV–vis absorption spectra of the electrolyte at each potential after staining with indophenol blue indicator for 2 h, suggesting that the electrocatalytic NRR process can occur within −0.6 V to −0.8 V. For the CTAB-D-W_4MoO_3 catalyst, it can be observed that as the potential gradually becomes negative, the NH_3 production rate presents a trend of first increasing and then decreasing, achieving the maximum NH_3 production rate at −0.70 V, reaching 60.77 μg h^{-1} $mg^{-1}{}_{cat.}$. The Faraday efficiency (FE) gradually decreases with the decrease of potential, with the highest FE at −0.60 V of 56.42%. This phenomenon is attributed that under a relatively negative applied potential, protons occupy more active sites, so that competitive hydrogen evolution reaction occupies the dominant position, which hinders the adsorption of N molecules on the surface of the catalyst.

Due to the peak ammonia production rate of CTAB-D-W_4MoO_3 catalyst at −0.70 V, the durability of this catalyst material was further studied at this potential. The chemical stability and durability of CTAB-D-W_4MoO_3 catalyst were evaluated by cyclic and long-term electrolytic tests respectively. Five cycle tests were conducted at −0.70 V, and there was no obvious fluctuation in ammonia production rate and Faraday efficiency (Fig. 3c), which proved that CTAB-D-W_4MoO_3 catalyst had excellent electrochemical stability. Meanwhile, a long-term electrocatalytic nitrogen reduction process was conducted at −0.70 V for 18 h, during which the current density did not significantly decrease (Fig. 3d), further demonstrating the good durability of the catalyst. The SEM and EDS mapping images of the CTAB-D-W_4MoO_3 catalyst after long-term testing showed that the morphology of the catalyst is relatively intact and there is no obvious change (Figs. S9 and S10 in Supporting information). In addition, according to the time-varying curves of current density at different potentials, it can be seen that the current density keeps on stable within −0.60 V to −0.80 V, indicating the good stability of the catalyst (Fig. S11 in Supporting information).

CTAB-W_4MoO_3 nanowires without oxygen vacancies and CTAB-H-W_4MoO_3 nanowires under N_2 calcination were prepared as comparison samples, respectively, and the NRR properties were measured. The ammonia production rate and FE of CTAB-W_4MoO_3 (20.26 μg h^{-1} $mg^{-1}{}_{cat.}$ and 17.1%) and CTAB-H-W_4MoO_3 (32.85 μg h^{-1} $mg^{-1}{}_{cat.}$ and 18.78%) (Fig. 3e) were both significantly lower than those of CTAB-D-W_4MoO_3 NWs (60.77 μg h^{-1} $mg^{-1}{}_{cat.}$ and 32.25%), and superior to most typical catalysts (Table S2 in Supporting information). Furthermore, In the electrochemical impedance spectroscopy (EIS) test results (Fig. S12 in Supporting information), the impedance radius of CTAB-D-W_4MoO_3 catalyst containing oxygen defects is significantly smaller than that of CTAB-W_4MoO_3, indicating that CTAB-D-W_4MoO_3 has a faster surface electron migration rate and can realize electron transfer. To further confirm the origin of NH_3, the ^{15}N isotopic test was conducted on CTAB-D-W_4MoO_3. As shown in Fig. 3f, a triple peak corresponding to $^{14}N_2$ and a double peak at $^{15}N_2$ appeared, confirming that the ammonia originated from the supplied nitrogen. The excellent performance of CTAB-D-W_4MoO_3 catalyst is further demonstrated by the use of two ammonium detection methods (Nessler's reagent method and Indophenol blue method, Fig. S13 in Supporting information).

In comparison of the absorbance of the electrolyte before and after the reaction, no by-product N_2H_4 is found, further indicating that CTAB-D-W_4MoO_3 catalyst has excellent selectivity (Fig. S14 in Supporting information). To exclude contamination of the electrolyte itself, we first detect NH_4^+ in the electrolyte before and after introducing N_2 for 30 min. The corresponding UV–vis spectrum is shown in Fig. S15a (Supporting information). The presence of NH_4^+ is not found, suggesting that the experimental results are not affected by impurity contamination. Fig. S15b (Supporting information) shows the UV–vis absorption spectrum of the 2 h electrolysis process at −0.70 V *vs.* RHE without catalyst loading on the working electrode. It can be seen that there was no NH_3 generation during this process, indicating that the CTAB-D-W_4MoO_3 catalyst catalyzed the generation of ammonia. In addition, to check that all NH_3 measured in the cathode chamber after the experiment was generated by the electrocatalytic nitrogen reduction process, electrocatalytic nitrogen reduction tests were conducted in Ar-saturated (−0.70 V) and N_2-saturated (at an open circuit potential) electrolyte. Figs. S15c and d (Supporting information) show the corresponding UV–vis absorption spectra under two test con-

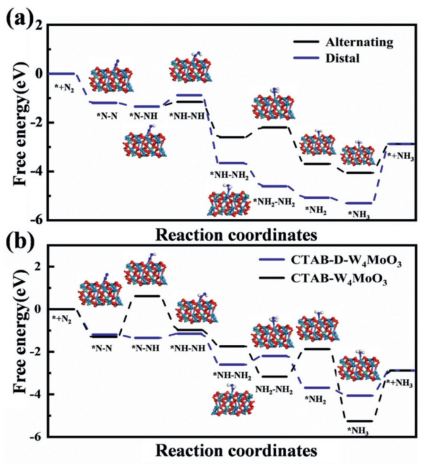

Fig. 4. (a) Reaction free energy pathways of NRR on CTAB-D-W_4MoO_3. (b) Free energy diagram of the NRR along the alternative pathway on CTAB-D-W_4MoO_3 and CTAB-W_4MoO_3.

ditions, indicating that NH_3 was not detected under either condition. This result indicates that all previously detected NH_3 comes from the NRR process. All the blank control experiments mentioned above have confirmed that the generated NH_3 comes from the electrocatalytic NRR process carried out by introducing nitrogen gas, rather than interference from the environment, reactor, or reactants.

DFT calculations are used to examine possible NRR pathways on CTAB-D-W_4MoO_3 (Fig. 4a). It can be seen that after the first step of hydrogenation, the *N-NH intermediate can be further hydrogenated through distal and alternative pathways, respectively. According to the Gibbs free energy diagram, the potential-determining step (PDS) of both pathways is *N-NH → *NH–NH. Due to the tendency of the alternative pathway towards lower energy (0.19/0.47 eV), the second hydrogenation step is achieved by the alternative pathway. The optimized geometries and the corresponding free energy changes of each step for CTAB-D-W_4MoO_3 and CTAB-W_4MoO_3 are shown in Fig. 4b. For the first step of hydrogenation (*N-N→*N-NH), the process on CTAB-D-W_4MoO_3 is a downhill pathway with ΔG=−0.15 eV, significantly lower than the process on CTAB-W_4MoO_3 (ΔG=1.90 eV), thus facilitating the further progress of the NRR process. Therefore, we conclude that the introduction of O vacancies in CTAB-D-W_4MoO_3 can reduce the energy barrier formed by the intermediate of *N-NH, facilitate the activation and further hydrogenation of *N-N, promote the NRR process, and improve the NRR performance.

In conclusion, the well-defined W_4MoO_3 nanowires rich in OVs (CTAB-D-W_4MoO_3 NWs) are constructed and prepared with the assistance of surfactant CTAB. CTAB-D-W_4MoO_3 NWs exhibit a high activity and selectivity with an NH_3 yield of 60.77 μg h^{-1} $mg^{-1}_{cat.}$ at −0.70 V and a FE of 56.42% at −0.60 V, outperforming CTAB-W_4MoO_3 NWs (NH_3 yield: 20.26 μg h^{-1} $mg^{-1}_{cat.}$; FE: 17.1%). Meanwhile, CTAB-D-W_4MoO_3 NWs also show excellent electrochemical stability. The outstanding NRR performance of CTAB-D-W_4MoO_3 NWs is primarily ascribed to the customized electronic structure, rich active sites, high conductivity and large specific surface area. DFT calculations confirm that the introduction of O vacancies in CTAB-D-W_4MoO_3 reduces the energy barrier formed by the intermediate of *N-NH, which facilitates the activation and further hydrogenation of *N-N, promotes the NRR process, and improves the NRR performance. This study provides a rational design of high-performance electrocatalysts.

Declaration of competing interest

The authors declare that they have no known competing financial interests or personal relationships that could have appeared to influence the work reported in this paper.

CRediT authorship contribution statement

Jincheng Zhang: Writing – review & editing. **Mengjie Sun:** Writing – original draft. **Jiali Ren:** Writing – original draft. **Rui Zhang:** Writing – original draft. **Min Ma:** Validation. **Qingzhong Xue:** Writing – review & editing. **Jian Tian:** Writing – review & editing.

Acknowledgments

This work is supported by the National Natural Science Foundation of China (No. 51872173) and Natural Science Foundation of Shandong Province (No. ZR2022JQ21).

Supplementary materials

Supplementary material associated with this article can be found, in the online version, at doi:10.1016/j.cclet.2024.110491.

References

[1] T. Wu, M.M. Melander, K. Honkala, ACS Catal. 12 (2022) 2505–2512.
[2] Z. Wang, J. You, J. Li, et al., ChemistrySelect 8 (2023) e202301199.
[3] M. Sun, C. Ma, M. Ma, et al., Mater. Today Phys. 30 (2023) 100945.
[4] Y. Zhao, J. You, L. Wang, et al., Int. J. Hydrogen Energy 46 (2021) 39146–39182.
[5] J.J. Li, J.H. You, Z.W. Wang, et al., J. Mater. Sci. 58 (2023) 10274–10287.
[6] X. Chen, S. Zhang, X. Qian, et al., Appl. Cataly. B: Environ. 310 (2022) 121277.
[7] Q. Wang, X. Xue, Y. Lei, et al., Small 16 (2020) 2001571.
[8] D. Chen, J. Lan, F. Xie, et al., Chem. Eng. J. 475 (2023) 146137.
[9] X. Li, J. You, J. Li, et al., ChemCatChem 16 (2024) e202301108.
[10] X. Qian, C. Ma, U.B. Shahid, et al., ACS Catal. 12 (2022) 6385–6393.
[11] X. Wang, M. Luo, J. Lan, et al., Adv. Mater. 33 (2021) 2007733.
[12] G. Liu, R. Yao, J. You, et al., Mater. Today Commun. 39 (2024) 109052.
[13] X. Qian, Y. Wei, M. Sun, et al., Chin. J. Catal. 43 (2022) 1937–1944.
[14] W. Li, C. Zhang, M. Han, et al., ACS Appl. Mater. Interfaces 11 (2019) 44186–44195.
[15] H. Huang, L. Xia, X. Shi, et al., Chem. Commun. 54 (2018) 11427–11430.
[16] W. Xu, G. Fan, J. Chen, et al., Angew. Chem. Int. Ed. 59 (2020) 3511–3516.
[17] J. Li, W. Wang, W. Chen, et al., Nano Res. 11 (2018) 4774–4785.
[18] Q. Zhang, J. You, X. Zhang, et al., Energy Fuels 38 (2024) 6659–6678.
[19] Q. Wang, Y. Lei, D. Wang, et al., Energy Environ. Sci. 12 (2019) 1730–1750.
[20] Z.W. Wang, J.H. You, J.J. Li, et al., Catal. Sci. Technol. 13 (2023) 274–296.
[21] Y. Zhao, J.H. You, Z.Y. Wang, et al., Inter. J. Hydrogen Energy 70 (2024) 599–605.
[22] L. Luo, B. Wang, J. Wang, et al., Phys. Chem. Chem. Phys. 23 (2021) 16658–16663.
[23] T. He, S.K. Matta, A. Du, Phys. Chem. Chem. Phys. 21 (2019) 1546–1551.
[24] X. Tang, J. Liu, K. Zhan, et al., Chem. Asian J. 15 (2020) 2984–2991.
[25] J. Han, X. Ji, X. Ren, et al., J. Mater. Chem. A 6 (2018) 12974–12977.
[26] L. Zhang, X. Ji, X. Ren, et al., Adv. Mater. 30 (2018) 1800191.
[27] X. Ren, G. Cui, L. Chen, et al., Chem. Commun. 54 (2018) 8474–8477.
[28] L.L. Han, X.J. Liu, J.P. Chen, et al., Angew. Chem. Int. Ed. 58 (2019) 2321–2325.
[29] H. Cheng, L.X. Ding, G.-F. Chen, et al., Adv. Mater. 30 (2018) 1803694.
[30] X. Zhang, Y. Guo, J. Tian, et al., Appl. Catal. B: Environ. 232 (2018) 355–364.
[31] G. Zhang, Q. Ji, K. Zhang, et al., Nano Energy 59 (2019) 10–16.
[32] X. Zhong, Y. Sun, X. Chen, et al., Adv. Funct. Mater. 26 (2016) 5778–5786.
[33] F. Shen, W. Jiang, G. Qian, et al., J. Power Sources 458 (2020) 228014.
[34] J. Wang, K. Chang, Z. Sun, et al., Appl. Catal. B: Environ. 251 (2019) 162–167.
[35] Y. Sun, X. Hu, W. Luo, et al., ACS Nano 5 (2011) 7100–7107.
[36] Z. Guo, Q. Ma, Z. Xuan, et al., RSC Adv. 6 (2016) 16730–16735.